THE JOURNAL OF PHYSICAL CHEMISTRY C
A JOURNAL OF THE AMERICAN CHEMICAL SOCIETY

pubs.acs.org/JPCC

Article

Correlating Electron−Phonon Coupling and In Situ High-Temperature Atomic-Scale Surface Structure at the Metallic Nb(100) Surface by Helium Atom Scattering and Density Functional Theory

Caleb J. Thompson, Michael F. Van Duinen, Michelle M. Kelley, Tomás A. Arias, and S. J. Sibener*

Cite This: *J. Phys. Chem. C* 2024, 128, 6149−6157

Read Online

ACCESS | Metrics & More | Article Recommendations

ABSTRACT: Helium (He) atom scattering (HAS) simultaneously measured the surface electron−phonon coupling (EPC, SEPC) constant (λ, λ_S) and in situ high-temperature atomic-scale surface structure of the unreconstructed, metallic Nb(100) surface. The Nb(100) surface λ_S is 0.50 ± 0.08, and its atomic-scale surface structure is confirmed. The λ_S measured for the Nb(100) surface is ∼1/2 the reported bulk Nb λ values. The significance of Nb(100)'s diminished EPC was elucidated by estimating relevant superconducting properties from the measured λ_S, surface Debye temperature, known material parameters, and well-established equations. Density functional theory (DFT) with local averaging agrees well with the HAS data. A critical temperature (T_C) of 1.4−3.6 K, a superheating field (H_{sh} at 2 K) ≤ 0.16 T, and a superconducting gap (at 2 K) ≤ 1.0 meV were estimated from these measurements. These results indicate that the Nb(100) surface has decreased superconducting properties relative to the bulk. This study shows that these effects may also be due to the interface itself even without oxygen. These results contain the first λ measured for the metallic Nb(100) and any Nb surface. These measurements begin a fundamental understanding of the atomic-scale surface structure's effect on EPC and superconductivity in Nb.

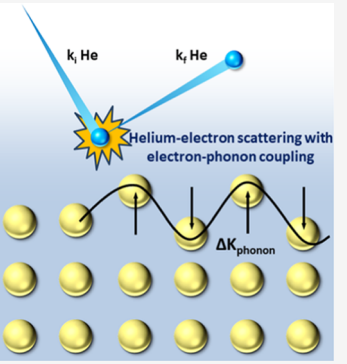

1. INTRODUCTION

Niobium is the current material of choice for superconducting radio frequency (SRF) cavities in particle accelerators. Both Nb's normal and superconducting state properties have led the material to its ubiquitous use and extensive study in SRF cavities.[1−4] Nb's relatively high ductility allows for facile manufacture of optimal cavity geometries for relatively high quality (Q) factors and accelerating gradients.[1−5] Additionally, pure Nb's relatively high thermal conductivity facilitates effective cooling, necessary to enter and maintain Nb's superconducting state.[1−3] Nb's superconducting state's relatively high critical temperature (T_C) and low RF surface resistance (R_s) contribute significantly to Nb SRF cavities' high Q factors at attainable operating temperatures.[1,4] Since the RF fields only penetrate through the first 40−100 nm of the cavity surface, SRF cavity performance depends critically upon the surface chemistry and surface quality.[1,6] Thus, the surface preparation of SRF cavities must be carefully designed and implemented. Furthermore, the superconducting state's unique behavior at these surfaces results from SRF cavity preparation techniques.[4,7−11] However, fundamental studies correlating the atomic-scale surface structure with changes in the superconducting state remain unexplored. How does the surface modify the physical properties driving the formation of the superconducting state and its favorable properties? A deeper understanding of atomic-scale surface structure's effect on the well-known superconducting state of the bulk would reveal the mechanisms determining which SRF cavity preparations aid or hinder the performance of a cavity. Additionally, since extensive research on Nb and Nb SRF cavities has allowed them to approach their fundamental limits of operation, the search has begun for new materials and cavity treatments to further reduce R_s, maximize the superheating field (H_{sh}), minimize power loss, and optimize overall performance.[5,7,8,11,12] Due to ≤100 nm penetration depth of RF fields in typical Nb SRF cavities, changes in the surface significantly affect cavity performance.[1,5,6] In fact, surface defects, inhomogeneities, and impurities limit cavity quality factors and operating temperatures, holding back a variety of promising new SRF cavity materials.[4,5,7,9,10,13,14] While well-studied, the evolution of surface defects remains a challenging part of the SRF cavity treatment design and implementation. An understanding of the evolution of surface defects and their resulting effects on superconductivity at the surface remains elusive. While the (3 × 1)-O has been shown to be stable and

Received: February 7, 2024
Revised: March 12, 2024
Accepted: March 18, 2024
Published: April 2, 2024

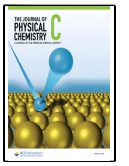

https://doi.org/10.1021/acs.jpcc.4c00852
J. Phys. Chem. C 2024, 128, 6149−6157

well-ordered up to ∼1130 K under SRF cavity preparations, a foundational understanding of the interface must begin with the metallic, unreconstructed surface.[15] Understanding how specific atomic-scale surface structures arising from distinct SRF cavity preparations impact the accelerator's performance and energetic efficiency would enable SRF cavity surfaces by design. In order to progress to this point, we must first understand the effect of the Nb surface structures on the material's superconducting properties by investigating the effects of surface treatments and their resulting surface structures.

Electron−phonon coupling (EPC) in Nb is responsible for the formation of its superconducting state.[1,16−19] The EPC constant (λ) is a dimensionless constant that quantifies the effective strength of electron−phonon interactions in a material.[19] This constant then determines many superconducting properties such as the critical temperature (T_C) and superconducting gap.[1,17,19] We will utilize helium (He) atom scattering's (HAS) unique capability for in situ high-temperature measurements of both surface structure and surface EPC (SEPC) constant (λ_S) to connect atomic-scale surface structure with its effect on λ_S and thus surface superconductivity. We have demonstrated this capability by measuring λ_S and atomic-scale surface structure simultaneously on the unreconstructed Nb(100) surface. While the Nb(100) surface structure and phonon band structure has been measured previously and calculated recently by Kelley et al., the SEPC constant, λ_S, has not.[20−24]

Furthermore, these results have begun building a necessary foundational understanding of the effects of the atomic-scale surface structure on superconductivity. With this understanding in hand, we plan to investigate variations in atomic-scale surface structure to reveal their effects on the surface superconductivity. Because this is the first measurement of SEPC at the Nb(100) surface, much remains to be known about the SEPC of Nb surfaces from changes in the surface composition and structure. However, many substantial studies of the EPC in bulk Nb have been made.[22,23,25−31] The EPC of bulk Nb has been measured by electronic Raman scattering (1.15),[28] proximity electron tunneling spectroscopy (1.04 ± 0.06),[32,33] femtosecond pump−probe measurements (1.16 ± 0.11),[30] and calculated with McMillan's well-known expression for T_C from accompanying measurements of appropriate normal-state parameters (0.92).[17,18,23]

Atomic and molecular beam scattering techniques have been used to investigate structure and vibrational dynamics of surfaces since the 1920s.[32−34] Supersonic He beams are suited to study surfaces due to their lack of penetration into the bulk, chemical inertness, and remarkably narrow velocity distributions.[34,35] The de Broglie wavelength and narrow momentum distribution of He atoms allow for precise measurements of the atomic-scale structure.[36,37] The momentum and energy of He atoms are well-matched to those of surface phonons, giving HAS a unique ability to measure and resolve low-energy phonon modes.[34−39] Recently, the role of SEPC in the He-surface scattering event has been elucidated and theoretically described for single phonon modes and thermally excited phonons in the high-temperature limit of many types of surfaces.[40−50]

While the derivation of the formula for λ_S differs for each kind of surface, including metals, metallic layers, 2D materials, and topological insulators, the concept of an electron mediated interaction between He and phonon states is present in all.[40−50] The He atoms scatter off of the surface electron density, and within good approximation, scattering repulsive potential is directly proportional to the electron density for metallic surfaces.[51] While He scatters off of the electron density, energy is exchanged between the He atom and the lattice of the crystal surface through phonon creation and annihilation events.[34,37,48] This energy exchange is mediated by the electron density at the surface and has been formulated for a variety of surfaces, especially metallic surfaces.[40−50] Recent work has expanded this formulation to show that the Debye−Waller (DW) factor is directly proportional to the SEPC constant (λ_S), which was accomplished starting from the distorted-wave Born approximation, using second-order perturbation theory to define electron−phonon matrix elements, and adopting additional yet reasonable approximations.[19,48−50] The DW factor is a multiplicative factor in all scattered intensities that describes thermal attenuation of the He atom's scattering intensity.[36,37,48] Traditionally, the DW factor accounted for the thermal excitation of phonons with appreciable displacements at the surface; however, these recent developments elucidated the mediation of thermally excited phonons and scattered He via the electron density.[36,48−50] Simply put, the thermal energy of the surface excites phonons at or near enough to the surface that they disturb the surface electron density which then reduces the coherence of the scattered He and measured HAS intensity.[48]

The work presented herein provides the first measurement of λ on the metallic, unreconstructed Nb(100) surface and any other Nb surface. Furthermore, it presents in situ high-temperature atomic-scale surface structure measurements made simultaneously with the λ_S measurement. This work utilizes and demonstrates HAS's unique capability for in situ high-temperature measurements of both the surface structure and the λ_S to connect the atomic-scale surface structure with its effect on λ and, thus, superconductivity. This capability unlocks the potential elucidation of the changes to the surface by oxides, carbon impurities, N doping, Sn alloying, and other SRF cavity preparations.

2. METHODS

Measurements were performed, and the crystal surface was prepared in an ultrahigh vacuum (UHV) scattering instrument. The instrument has been detailed elsewhere, but is summarized below.[15,52−54] The instrument was composed of three main sections: a differentially pumped beam source, a sample chamber, and a differentially pumped rotating detector. The sample surface was prepared and altered, and all measurements were made in situ within the sample chamber. A supersonic atomic or molecular beam was created by expansion from a 15 μm nozzle cooled with a closed-cycle He refrigerator. A skimmer extended through the Mach disk into the zone of silence, extracting a supersonic atomic or molecular beam. In the next differentially pumped chamber, the beam passed through a mechanical chopper for pulse modulation. The resulting supersonic beam was nearly monoenergetic ($\Delta v/v \leq 1\%$). This beam had a spot size of ∼4 mm on the 1 cm sample, scattering into 2π steradians. A triply differentially pumped, computer-controlled, rotatable detector arm collected scattered atoms or molecules. Between the differentially pumped detector regions, the probe atoms or molecules were ionized by electron bombardment, mass selected using a quadrupole mass spectrometer, and detected with an electron multiplier, followed by pulse counting electronics. The flight

https://doi.org/10.1021/acs.jpcc.4c00852
J. Phys. Chem. C 2024, 128, 6149−6157

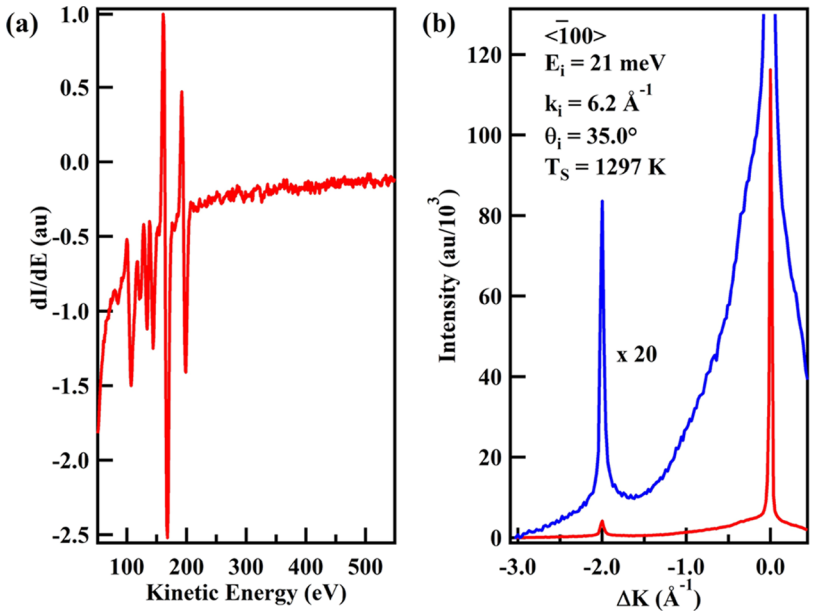

Figure 1. Representative (a) Auger electron spectrum and (b) He atom diffraction spectrum for the clean, unreconstructed Nb(100) surface along the <$\bar{1}$00> symmetry axis. In panel (a), the primary Nb peak is evident at 167 eV and the secondary Nb peak at 192 eV. There is an absence of C (270 eV), N (379 eV), and O (503 eV) peaks, indicating a clean Nb surface. In panel (b), there is only the first-order diffraction peak. This peak is sharp and weak relative to the specular reflection, indicating a smooth, well-ordered metallic surface.

path was 1.528 m, the sum of the chopper-to-sample path was 0.500 m, and the sample to ionizer path was 1.028 m. For our experiments, we used He as our probe, scattering from a Nb(100) surface with a supersonic He atomic beam.

Diffraction scans were obtained by square-wave beam modulation, with a 50% duty cycle and rotating the detector at 0.2° increments with fixed incident angle and energy, with an overall instrument angular resolution of 0.20°. The beam was characterized by time-of-flight (TOF) measurements made with a single-slit chopping 1% duty cycle pattern. The Nb(100) crystal was mounted on a six-axis manipulator within the HAS instrument's sample chamber. This manipulator enables control over the incident angle, θ_i, azimuthal angle, ϕ, and tilt, χ, with respect to the scattering plane. Electron bombardment heating and a closed-cycle He refrigerator modulated the sample temperature within a range of 300–2300 K. Surface Preparation Laboratory (The Netherlands) provided the Nb(100) sample (99.99% purity, ∼0.1° cut accuracy), which we then cleaned in the HAS instrument by cycles of annealing and flashing up to 2300 K, in addition to sputtering with 1 keV Ne^+ ions (3 μA maximum). Impurities identified by in situ AES were C, B, S, and N; these were removed by the combination of annealing, flashing, and sputtering. We continued the cleaning cycles until only Nb was present on the surface, as confirmed by AES, and until the surface was well-ordered enough for high-intensity He diffraction. Due to the annealing (∼2300 K), flashing (∼2300 K), and sputtering process described above, the unreconstructed Nb(100) surface formed naturally and spontaneously. The Nb(100) surface structure and cleanliness was confirmed with AES, low-energy electron diffraction (LEED), and He diffraction. During data collection, the Nb sample was periodically flashed to ∼2300 K to eliminate unwanted surface adsorbates. Debye–Waller data were obtained by aligning the crystal at each surface temperature and taking diffraction scans across the specular peak. Each Debye–Waller measurement consisted of varying surface temperature up and then down a chosen temperature range, aligning the crystal and taking a diffraction scan over specular. These measurements were taken from the lower limit, ∼1400 K, of the chosen temperature range to the upper limit, ∼1750 K, and then immediately back down to the lower limit. The lower temperature limit was determined as the lowest temperature free of substantial background gas adsorption in the time that it took to align and take a diffraction scan. The crystal and mount thermally equilibrated for ∼5 min and then was aligned before every diffraction scan. The thermal equilibration time for the crystal and mount was determined by comparing thermocouple measurements on the mount to pyrometer measurements of the crystal.

To theoretically study the Nb(100) surface, we performed density functional theory (DFT) calculations using open-source planewave software JDFTx.[55,56] We implemented norm-conserving pseudopotentials[57] and calculated the electronic states for the outer electrons of niobium ($4p^6 5s^2 4d^3$) at an effective temperature of 20 milli-Hartree using a Fermi function to determine electronic occupancies. The exchange–correlation energy was approximated using the Perdew–Burke–Ernzerhof functional revised for solids (PBEsol).[58] Our calculations employed planewave cutoff energies of 30 Hartree and 200 Hartree for the electronic wave functions and density, respectively. We computed properties of a 10-layer slab of niobium with (100) surface termination in a cell that is 42.33 Å long along the surface-normal direction and truncated Coulomb potentials to increase the accuracy of calculated surface properties.[59] We calculated a lateral lattice constant for Nb(100) at 3.30 Å, in good agreement with the experimental measurement of 3.29 Å.[60] We calculated phonon properties using the finite-difference supercell method, perturbing atoms by ∼0.4 to 0.5a_0 to calculate the real space interatomic force constant matrix directly.[61] Interatomic force constant matrices for Nb(100) were evaluated in a 3 × 3 × 1 supercell with a k-space sampling density equal to the unit cell's sampling of 12 × 12 × 1 k-points.

https://doi.org/10.1021/acs.jpcc.4c00852
J. Phys. Chem. C 2024, 128, 6149–6157

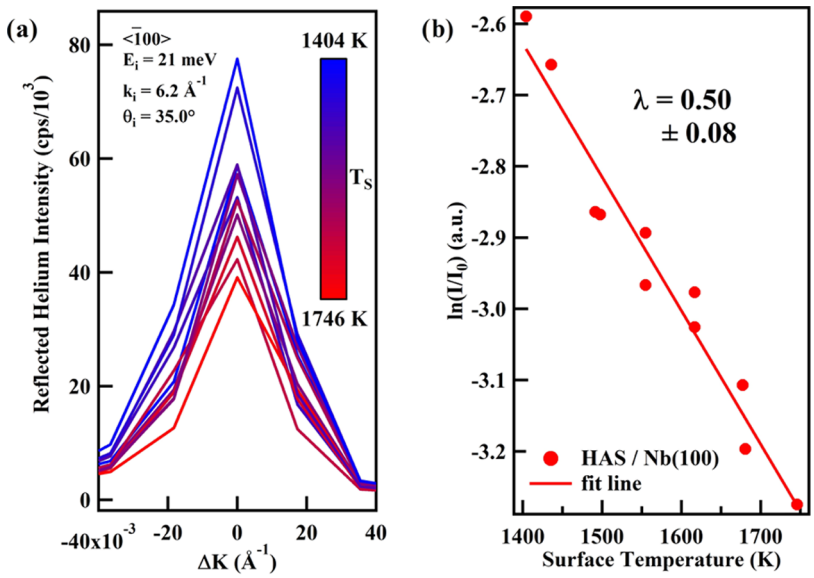

Figure 2. Thermal attenuation of the specular peak is observed in panel (a), where diffraction scans through the range were taken proceeding up the temperature range to 1746 K and then back down to 1404 K. The surface structure and cleanliness was confirmed with HAS diffraction and AES immediately before and after the measurement. The intensity values are taken from these specular reflections and plotted in panel (b). In panel (b), the ln of specular intensity is plotted versus surface temperature. The linear fit provides I_0 (intensity at 0 K) from the y-intercept fitting parameter and a slope fitting parameter equal to $\mathrm{d}\ln I_{00}/\mathrm{d}T_S$. From this slope and tabulated values for Nb's work function, number of free electrons per atom, and Fermi wavevector, we calculate $\lambda = 0.50 \pm 0.08$ for the Nb(100) surface. The error is propagated from the fit error of the slope fitting parameter. Furthermore, we also extract the surface Debye temperature of 369 ± 11 K from these data, verifying that the system in the high-temperature regime of the Bose−Einstein phonon population function is required for eq 3. Additionally the Debye temperature is used in calculating T_C from the measured λ and the McMillan equation.

3. RESULTS AND DISCUSSION

The clean metallic unreconstructed Nb(100) surface was prepared and confirmed with HAS diffraction and AES as shown in Figure 1(a,b), respectively. Figure 1(a) contains a diffraction scan taken at 1297 K along the <$\bar{1}$00>, $\overline{\Gamma X}$ azimuthal direction. Each peak occurs when the von Laue condition holds true, or when

$$\Delta K = k_i(\sin\theta_i - \sin\theta_f) = G_{mn} \tag{1}$$

where the surface-parallel component of the He wavevector k_i changes by ΔK; the initial and final scattering angles, relative to surface normal, are θ_i and θ_f, respectively; and G_{mn} is a linear combination of reciprocal surface lattice vectors.[16,36,37] The scan shows an intense, narrow specular peak ($\theta_i = \theta_f$) at $\Delta K = 0$ and the first-order ($0\bar{1}$) diffraction peak at $\Delta K = -2.000$ Å^{-1}, just slightly beyond the expected -1.904 Å^{-1}.[20,21] This diffraction peak shifted slightly above and below the expected value after each preparation, indicating some lattice compression and expansion.[62] The specular peak is ∼28 times the size of the first-order diffraction peak, typical of a smooth metal surface with relatively flat electronic corrugation.[48,63] The absence of oxygen in the Auger data is corroborated by the absence of any superlattice peaks along this symmetry direction in the diffraction scan.[15,21,54]

Thermal attenuation of the specular peak occurs due to thermally excited phonons disturbing the electron density at the surface. This thermal attenuation follows the following relation

$$I(T_S) = I(0)\mathrm{e}^{-2W(T_S)} \tag{2}$$

where I is the measured He scattered intensity and $2W$ is the DW factor.[36,64] The traditional definition of the DW factor is

$$2W(T_S) = \langle(\Delta k \cdot u(T_S))^2\rangle \tag{3}$$

where Δk is the change in wavevector of the scattered He and u atomic displacement of the surface atoms.[64] However, recently, Manson et al. has derived the relationship between 2W and the surface EPC constant, yielding the approximation

$$\lambda_{HAS} \cong -\frac{\mathrm{d}\ln I_{00}}{k_B \mathrm{d}T_S}\frac{\phi}{6Z}\frac{k_F^2}{k_{iz}^2} \tag{4}$$

where I_{00} is the intensity of the specular reflection, ϕ is the work function, Z is the number of free electrons per atom, k_F is the Fermi wavevector, and k_{iz} is the surface perpendicular (z) component of the He incident wavevector.[49,50] The DW diffraction scans were taken over the specular peak at a variety of temperatures. These temperatures were chosen to be above any significant adsorption of background gases. These diffraction scans were taken from temperatures ∼1400 to ∼1750 K for a variety of beam energies.

The data used for the slope, $\frac{\mathrm{d}\ln I_{00}}{k_B \mathrm{d}T_S}$, which determines λ_S through eq 4, were measured taking particular care for surface cleanliness. Specifically, these EPC DW data (Figure 2) were obtained while confirming a clean Nb(100) surface structure through cleanliness with HAS diffraction and AES prior to and after each DW measurement. This procedure ensured no impurities interfered with the measurement.

This slope and tabulated values of the Fermi vector, work function, and number of free electrons per atom were used to calculate a λ_S of 0.50 ± 0.08 for the clean metallic Nb(100) surface.[16,49,50] The uncertainty in this value is propagated from the error in the linear fit of the data.

This is the first recorded value of λ for any Nb surface and specifically the Nb(100) surface. The recorded λ values for

https://doi.org/10.1021/acs.jpcc.4c00852
J. Phys. Chem. C 2024, 128, 6149−6157

bulk Nb are 1.15, 1.04, 1.16, and 0.92, almost twice the value at the Nb(100) surface we determine here.[22,23,25−31] This deviation shows that the Nb(100) surface reduces the level of electron phonon coupling at the surface relative to the bulk. This reduction indicates that the termination of the Nb lattice with a Nb(100) surface should be expected to significantly decrease the superconducting gap and increase the RF resistance relative to the bulk. In SRF cavities, the surface oxide is commonly thought to decrease the efficiency of Nb SRF cavities; surprisingly, these effects may be due to the termination of the lattice in addition to the effects of the oxygen.[1,14] This work begins to build a fundamental understanding of the effects of the surface.

In addition to this refined DW measurement of the clean Nb(100) surface, we obtained a variety of DW measurements with varying amounts of impurities, as measured by AES. These impurities did not affect surface structure, periodicity, order, or electronic corrugation, but they did affect Nb(100) SEPC. We concluded from further data analysis that these impurities must be at the subsurface. This ultimately meant that while these data were not appropriate to determine λ_S for a pure, metallic Nb(100) surface, they were ultimately appropriate to determine a He-surface attractive potential well depth, and they reveal linear trends between SEPC and impurity concentration. These data are summarized in Figure 3.

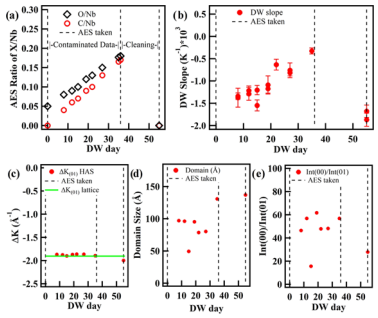

Figure 3. In panel (a), the AES ratios of O and C with Nb are plotted versus time (days). The blue lines mark when AES spectra were taken and the region between day 0 and day 36 was linearly interpolated to obtain the O and C ratio on each day. In panel (b), the DW slopes from each day were plotted versus time (days) showing a strong correlation with the O and C content. However, in plots (c), (d), and (e) the (01) diffraction peak dK, domain size, and ratio of (01) peak to the specular (00) peak, respectively, show no correlation with O and C content. The diffraction peak's dK (c) show that the periodic lattice spacing is uncorrelated with O and C content. The domain sizes (d), obtained from the specular (00) diffraction peak's fwhm, indicate that the surface order is uncorrelated with O and C content. Furthermore, the ratios of specular to the diffraction peak (e) demonstrate that the electronic corrugation at the surface is uncorrelated with O and C content.

Looking at the data in Figure 3, one may observe the correlation between the O and C content with the DW slope but not in the diffraction peak location, specular to the diffraction peak ratio, or domain size (extracted from the fwhm of the specular peak). The latter three properties are specific to surface structure, periodicity, order, and electronic corrugation, but the DW slopes involve surface vibrations that are also affected by the subsurface.[65,66] Since AES probes both the surface and a few layers into the subsurface, and the DW slope is the only surface property we measured that seems to be affected by the C and O impurities, we can conclude that these impurities must lie at the subsurface but not at the surface. If we take the DW data where the subsurface O and C content varies and extract λ_S, we see that there is an apparent diminishing of λ_S with accumulation of subsurface O and C impurities (Figure 4).

For the impure DW measurements, the subsurface O and C contents on each DW measurement were estimated by linearly interpolating between the two AES measurements on days 1 and 36 in Figure 3(a). While not the primary focus of this study, this effect is deserving of its own investigation in future work. Nonetheless, the data show that subsurface O and C apparently diminish λ_S and indicate that such subsurface impurities actively contribute to surface superconductivity and SRF cavity performance. In fact, the effect of interstitial O on bulk Nb's EPC has been measured in the range of 0−4% by Koch et al.[26] These amounts of interstitial O were observed to decrease the EPC linearly with accumulated interstitial O, much like the trend observed in Figure 4(a).

At beam energies from ∼17 to ∼35 meV, the acceleration due to the He-surface attractive potential well depth, D, is significant and must be taken into account. The Beeby approximation is commonly used to correct for this effect, taking into account the acceleration of the He atom as it approaches the surface before reaching its turning point.[34,36,37] In the Beeby approximation, the potential well depth is added to the surface perpendicular component of the incident He beam energy.[37] This quantity can be measured by expanding the traditional expression of the DW factor with standard kinematics. Upon substitution, restriction to specular scattering and rearrangement, the relation

$$\sigma = -\frac{\mathrm{d}(2W)}{\mathrm{d}T_S} = 4k_i^2 \frac{\mathrm{d}\langle u_z^2\rangle}{\mathrm{d}T_S}\left[\cos^2\theta_i + \frac{D}{E_i}\right] \tag{5}$$

is obtained, where σ is the negative slope of a DW linear plot, k_i is the He incident wavevector, θ_i is incident angle relative to surface normal, D is the He-surface potential well depth, and E_i is the He incident energy.[36,67] Thus, a fit of DW decay, σ, versus $E_i \cos^2\theta_i$ yields the He-surface attractive potential well depth and the first derivative of the mean-square displacement with respect to the surface temperature. We will choose DW measurements with the narrowest range of subsurface impurities at 3 beam temperatures and use them to obtain a He-surface attractive potential well depth (Figure 5). The data with subsurface impurities are appropriate for the well depth calculation since the attractive potential well depth is exclusively a surface phenomenon.

From the fitting parameters, we obtain a He-surface well depth of 5.8 with error due to varying subsurface impurities. Having an estimate for the well depth D allows us to correct our incident beam energy with the Beeby correction.

We use DFT calculations of the mean-squared displacement (MSD) of the surface atomic vibrations of Nb(100) to complement our HAS data from clean metallic Nb(100). Figure 6 shows the vertical mean-squared displacement (MSD) of the surface atomic vibrations of Nb(100) calculated with

$$\langle u_z^2\rangle = \frac{1}{N_Q}\sum_{Q\nu}[2n(\omega_{Q\nu}, T) + 1]\frac{\hbar\,|e_{Q\nu}^{0,z}|^2}{2M\omega_{Q\nu}} \tag{6}$$

https://doi.org/10.1021/acs.jpcc.4c00852
J. Phys. Chem. C 2024, 128, 6149−6157

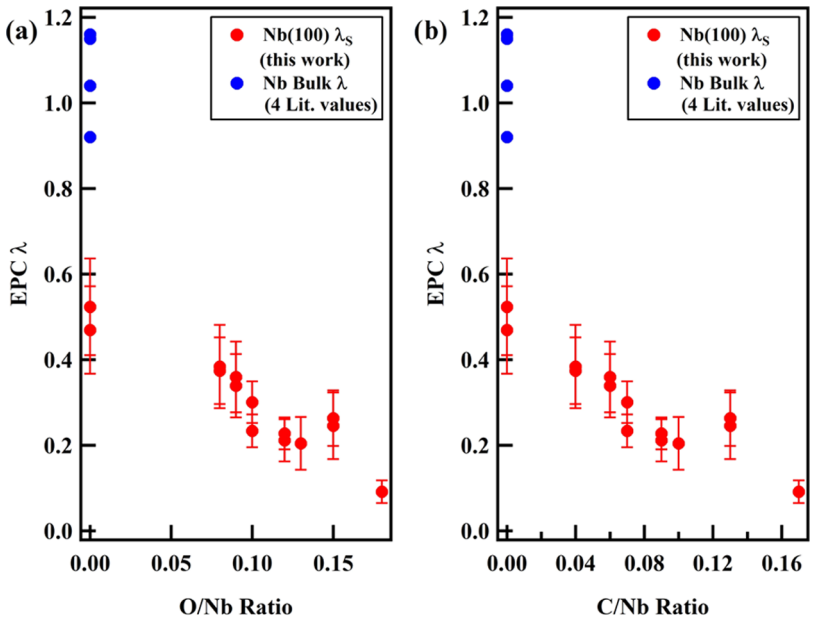

Figure 4. EPC constant was extracted from the DW slopes plotted in Figure 3(b) and plotted against the values of the O/Nb (a) and C/Nb (b). There is an apparent diminishing of λ_S with the accumulation of subsurface O and C impurities. While we have not intended to study or observe this effect, we have coincidentally observed it. This effect deserves its own investigation that is outside the scope of this paper. Nonetheless, the data show that subsurface O and C apparently diminish λ_S and indicate that such subsurface impurities actively contribute to surface superconductivity and SRF cavity performance.

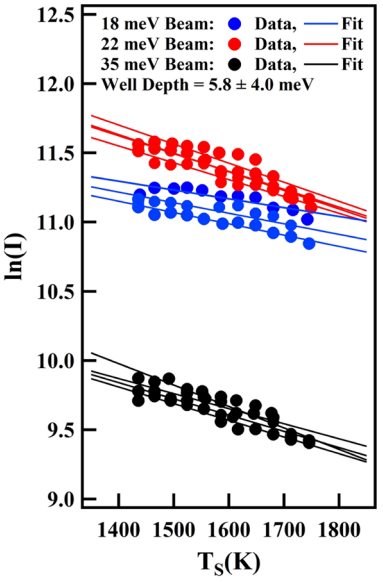

Figure 5. DW lines at 3 beam energies were selected for a relatively narrow range of subsurface impurities. These data provide the He-surface well depth of 5.8 meV with error due to varying subsurface impurities. Having an estimate for the well depth, D, allows us to correct our incident beam energy in the so-called Beeby correction.

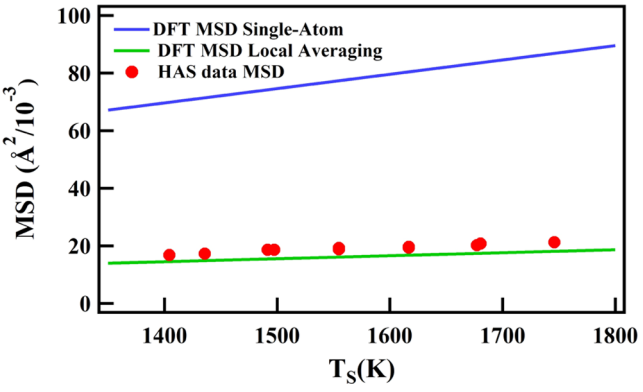

Figure 6. Upper theoretical curve (blue) shows the raw average of $\langle u_z^2 \rangle$ considering the one Nb atom of the monatomic crystal structure. The lower theoretical value (green) shows an effective MSD after averaging over the four surface atoms from the square unit cell, which accounts for the likelihood of the incident He atom interacting with more than one Nb atom due to the comparable distance between Nb surface atoms and the finite size of He. The HAS data (red dots) fall upon the DFT prediction for HAS scattering (green) confirming the HAS measurements of clean, unreconstructed Nb(100).

where the summation samples phonon modes ν at wavevectors $\mathbf{Q}$ throughout the surface Brillouin zone, $e_{Q\nu}^{0,z}$ is the component of the phonon eigenvector corresponding to the z-displacement of the surface niobium-atom of mass M, and the Bose factor $n(\omega_{Q\nu})$ weights the displacements of each sampled phonon mode at temperature T.[48] This quantity enters the traditional definition of the DW factor in eq 3.

The lower theoretical curve shows the raw average of $\langle u_z^2 \rangle$ considering the one Nb atom of the monatomic crystal structure. The upper theoretical curve shows an effective MSD after averaging over the four surface atoms from the square unit cell, which accounts for the likelihood of the incident He atom interacting with more than one Nb atom due to the comparable distance between Nb surface atoms and the finite size of He.[66] Using this locally averaged MSD and performing a least-squares fit of the well depth in the Beeby approximation, the predicted DW factor from this effective MSD would match the measured HAS DW data at a well depth of 9.5 meV. The HAS data fall within this region confirming the HAS measurements of clean, unreconstructed Nb(100).

To more deeply understand how this modification of the bulk λ would affect the surface's performance in an SRF cavity,

https://doi.org/10.1021/acs.jpcc.4c00852
J. Phys. Chem. C 2024, 128, 6149−6157

Table 1. Benchmark Superconducting Properties Were Estimated from Well-Used Equations Using EPC Constants and Tabulated Material Properties[a]

	λ EPC	T_C (K)	critical field (T)	superheating field (T)	band gap (meV)
Nb(100)	0.50	1.4−3.6	≤0.14	≤0.16	≤1.0
Nb bulk (refs22,23,25−31)	1.15, 1.04, 1.16, 0.92	9	0.21	0.25	2.8

[a]Superconducting properties were estimated for T = 2 K, using well-known tabulated values for Nb: London penetration depth = 40 nm, ξ = 27 nm, κ = 1.5, μ^* = 0.1−0.15, and critical field of 0.20 T at 0 K. The surface EPC and Debye temperature extracted from HAS data were used to estimate the values for the unreconstructed Nb(100) surface.

we estimate superconducting properties that are commonly used benchmarks for prospective SRF cavity materials.[1,12] The resulting values are compiled in Table 1.

We used Dynes' version of McMillan's equation as well as our measured surface Debye temperature and λ_S to estimate a T_C within the range of 1.4−3.6 K, significantly reduced from the bulk Nb value of 9 K.[1,17,19,68] A lower T_C ultimately corresponds to a lower superheating field H_{sh} of ≤0.16 T compared to the bulk value 0.25 T.[1,12,16,69] This means that superconducting states at the Nb(100) surface quench at lower magnetic fields than those in the bulk, reducing SRF performance.[4,69] We estimate the superconducting gap at 0 K and then, using λ_S and an empirical temperature dependence valid below T_C, estimate a superconducting gap at 2 K to be ≤1.0 meV, significantly reduced from 2.8 meV for bulk Nb at 2 K.[1,19,29,70] A smaller superconducting gap results in a higher R_S, a lower Q, and therefore a less efficient SRF cavity.[5,17] These theoretical estimates from our measured λ_S and surface Debye temperature as well as the measurements themselves show that the atomic-scale surface structure of Nb(100) significantly modifies the relevant properties of the superconducting state, decreasing the SRF cavity performance even without the presence of a deleterious oxide.

4. CONCLUSIONS

We have utilized He atom scattering's (HAS) unique capability for in situ high-temperature measurements of both the surface structure and the surface electron−phonon coupling (SEPC) constant, λ_S, to connect the atomic-scale surface structure with its effect on λ_S and thus superconductivity. We measured the λ_S and in situ high-temperature atomic-scale structure of the unreconstructed, metallic Nb(100) surface. The thermal attenuation of the specular reflectivity gave a λ_S of 0.50 ± 0.08, and He diffraction confirmed the unreconstructed metallic Nb(100) surface. These results give the first λ_S measured for the unreconstructed, metallic Nb(100) surface and any Nb surface. We find that SEPC, T_C, superconducting gap, and superheating field at operational temperatures are significantly reduced at the Nb(100) surface relative to those of the bulk Nb. While the Nb surface in SRF cavities is oxidized, this begins to build a needed, fundamental understanding of the effects of the surface on superconducting properties, and from there, we can begin to understand the changes to the surface by oxides, carbon impurities, N doping, Sn alloying, and other SRF cavity preparations. These measurements are the beginning of a fundamental understanding of atomic-scale surface structure's effect on EPC and superconductivity in Nb, enabling SRF cavity surfaces by design.

AUTHOR INFORMATION

Corresponding Author

S. J. Sibener − *The James Franck Institute and Department of Chemistry, The University of Chicago, Chicago, Illinois 60637, United States;* orcid.org/0000-0002-5298-5484; Email: s-sibener@uchicago.edu

Authors

Caleb J. Thompson − *The James Franck Institute and Department of Chemistry, The University of Chicago, Chicago, Illinois 60637, United States*

Michael F. Van Duinen − *The James Franck Institute and Department of Chemistry, The University of Chicago, Chicago, Illinois 60637, United States*

Michelle M. Kelley − *Department of Physics, Cornell University, Ithaca, New York 14853, United States*

Tomás A. Arias − *Department of Physics, Cornell University, Ithaca, New York 14853, United States*

Complete contact information is available at: https://pubs.acs.org/10.1021/acs.jpcc.4c00852

Notes

The authors declare no competing financial interest.

ACKNOWLEDGMENTS

S.J.S. and T.A.A. would like to acknowledge support from the U.S. National Science Foundation under Award PHY-1549132, the Center for Bright Beams, while S.J.S. also acknowledges support from the Air Force Office of Scientific Research Grant No. FA9550-19-1-0324 for fundamental studies of gas-surface energy transfer. Support from the NSF-Materials Research Science and Engineering Center at The University of Chicago, Grant No. NSF-DMR-2011854, also is gratefully acknowledged.

REFERENCES

(1) Padamsee, H.; Knobloch, J.; Hays, T. *RF Superconductivity for Accelerators*, Wiley Series in Beam Physics and Accelerator Technology; John Wiley & Sons, Inc.: Cornell University: Ithaca, NY, 1998.

(2) Padamsee, H.; Shepard, K. W.; Sundelin, R. Physics and Accelerator Applications of RF Superconductivity. *Annu. Rev. Nucl. Part. Sci.* **1993**, *43* (1), 635−686.

(3) Padamsee, H. The Science and Technology of Superconducting Cavities for Accelerators. *Supercond. Sci. Technol.* **2001**, *14* (4), R28.

(4) Posen, S.; Valles, N.; Liepe, M. Radio Frequency Magnetic Field Limits of Nb and Nb 3 Sn. *Phys. Rev. Lett.* **2015**, *115* (4), No. 047001.

(5) Posen, S. Understanding and Overcoming Limitation Mechanisms in Nb3Sn Superconducting Rf Cavities; Cornell University, 2015. https://www.classe.cornell.edu/rsrc/Home/Research/SRF/SrfDissertations/Posen_thesis.pdf (accessed Oct 2, 2022).

(6) Finnemore, D. K.; Stromberg, T. F.; Swenson, C. A. Superconducting Properties of High-Purity Niobium. *Phys. Rev.* **1966**, *149* (1), 231−243.

https://doi.org/10.1021/acs.jpcc.4c00852
J. Phys. Chem. C 2024, 128, 6149−6157

(7) Checchin, M.; Grassellino, A.; Martinello, M.; Melnychuk, O.; Posen, S.; Romanenko, A.; Sergatskov, D. *New Insight on Nitrogen Infusion Revealed by Successive Nanometric Material Removal; FERMILAB-CONF-18−762-TD*; Fermi National Accelerator Lab. (FNAL): Batavia, IL (United States), 2018; pp 2665−2667.
(8) Grassellino, A.; Romanenko, A.; Sergatskov, D.; Melnychuk, O.; Trenikhina, Y.; Crawford, A.; Rowe, A.; Wong, M.; Khabiboulline, T.; Barkov, F. Nitrogen and Argon Doping of Niobium for Superconducting Radio Frequency Cavities: A Pathway to Highly Efficient Accelerating Structures. *Supercond. Sci. Technol.* **2013**, *26* (10), No. 102001.
(9) Porter, R.; Arias, T.; Cueva, P.; Hall, D.; Liepe, M.; Maniscalco, J.; Muller, D.; Sitaraman, N. *Next Generation Nb3Sn SRF Cavities for Linear Accelerators*; JACOW Publishing: Geneva, Switzerland, 2019; pp 462−465.
(10) Ciovati, G.; Myneni, G.; Stevie, F.; Maheshwari, P.; Griffis, D. High Field Q Slope and the Baking Effect: Review of Recent Experimental Results and New Data on Nb Heat Treatments. *Phys. Rev. Accel. Beams* **2010**, *13* (2), No. 022002.
(11) Sitaraman, N. S.; Sun, Z.; Francis, B. L.; Hire, A. C.; Oseroff, T.; Baraissov, Z.; Arias, T. A.; Hennig, R. G.; Liepe, M. U.; Muller, D. A.; et al. Center for Bright Beams. Enhanced Surface Superconductivity of Niobium by Zirconium Doping. *Phys. Rev. Appl.* **2023**, *20* (1), No. 014064.
(12) Liarte, D. B.; Posen, S.; Transtrum, M. K.; Catelani, G.; Liepe, M.; Sethna, J. P. Theoretical Estimates of Maximum Fields in Superconducting Resonant Radio Frequency Cavities: Stability Theory, Disorder, and Laminates. *Supercond. Sci. Technol.* **2017**, *30* (3), No. 033002.
(13) Posen, S.; Hall, D. L. Nb3Sn Superconducting Radiofrequency Cavities: Fabrication, Results, Properties, and Prospects. *Supercond. Sci. Technol.* **2017**, *30* (3), No. 033004.
(14) Romanenko, A.; Grassellino, A.; Barkov, F.; Ozelis, J. P. Effect of Mild Baking on Superconducting Niobium Cavities Investigated by Sequential Nanoremoval. *Phys. Rev. Accel. Beams* **2013**, *16* (1), No. 012001.
(15) McMillan, A. A.; Graham, J. D.; Willson, S. A.; Farber, R. G.; Thompson, C. J.; Sibener, S. J. Persistence of the Nb(100) Surface Oxide Reconstruction at Elevated Temperatures. *Supercond. Sci. Technol.* **2020**, *33* (10), No. 105012.
(16) Ashcroft, N. W.; Mermin, N. D. *Solid State Physics; Brookes/Cole, a Part of Cengage Learning*, 1976.
(17) Tinkham, M. *Introduction to Superconductivity*; Robert E. Krieger Publishing Company, 1980.
(18) Bardeen, J.; Cooper, L. N.; Schrieffer, J. R. Theory of Superconductivity. *Phys. Rev.* **1957**, *108* (5), 1175−1204.
(19) Grimvall, G. *The Electron-Phonon Interaction in Metals*, Series of Monographs on Selected Topics in Solid State Physics; North-Holland Publishing Company, 1981; Vol. *16*.
(20) Hulpke, E.; Hüppauff, M.; Smilgies, D.-M.; Kulkarni, A. D.; de Wette, F. W. Lattice Dynamics of the Niobium (001) Surface. *Phys. Rev. B* **1992**, *45* (4), 1820−1828.
(21) An, B.; Fukuyama, S.; Yokogawa, K.; Yoshimura, M. Surface Structures of Clean and Oxidized Nb(100) by LEED, AES, and STM. *Phys. Rev. B* **2003**, *68* (11), No. 115423.
(22) Butler, W. H.; Smith, H. G.; Wakabayashi, N. Electron-Phonon Contribution to the Phonon Linewidth in Nb: Theory and Experiment. *Phys. Rev. Lett.* **1977**, *39* (16), 1004−1007.
(23) Shapiro, S. M.; Shirane, G.; Axe, J. D. Measurements of the Electron-Phonon Interaction in Nb by Inelastic Neutron Scattering. *Phys. Rev. B* **1975**, *12* (11), 4899−4908.
(24) Kelley, M. M.; Sundararaman, R.; Arias, T. A. Fully Ab Initio Approach to Inelastic Atom-Surface Scattering. *Phys. Rev. Lett.* **2024**, *132* (1), No. 016203.
(25) DeSorbo, W. Effect of Dissolved Gases on Some Superconducting Properties of Niobium. *Phys. Rev.* **1963**, *132* (1), 107−121.
(26) Koch, C. C.; Scarbrough, J. O.; Kroeger, D. M. Effects of Interstitial Oxygen on the Superconductivity of Niobium. *Phys. Rev. B* **1974**, *9* (3), 888−897.
(27) Gupta, M. Electronic Properties and Electron-Phonon Coupling in Zirconium and Niobium Hydrides. *Phys. Rev. B* **1982**, *25* (2), 1027−1038.
(28) Ponosov, Y. S.; Streltsov, S. V. Measurements of Raman Scattering by Electrons in Metals: The Effects of Electron-Phonon Coupling. *Phys. Rev. B* **2012**, *86* (4), No. 045138, DOI: 10.1103/PhysRevB.86.045138.
(29) Aynajian, P.; Keller, T.; Boeri, L.; Shapiro, S. M.; Habicht, K.; Keimer, B. Energy Gaps and Kohn Anomalies in Elemental Superconductors. *Science* **2008**, *319* (5869), 1509−1512.
(30) Brorson, S. D.; Kazeroonian, A.; Moodera, J. S.; Face, D. W.; Cheng, T. K.; Ippen, E. P.; Dresselhaus, M. S.; Dresselhaus, G. Femtosecond Room-Temperature Measurement of the Electron-Phonon Coupling Constant γ in Metallic Superconductors. *Phys. Rev. Lett.* **1990**, *64* (18), 2172−2175.
(31) Bennemann, K. H.; Garland, J. W.; Wolfe, H. C.; Douglass, D. H. *Theory for Superconductivity in D-Band Metals*; Rochester, New York (USA), 1972; pp 103−137.
(32) Wolf, E. L.; Zasadzinski, J.; Osmun, J. W.; Arnold, G. B. Proximity Electron Tunneling Spectroscopy I. Experiments on Nb. *J. Low Temp. Phys.* **1980**, *40* (1), 19−50.
(33) Arnold, G. B.; Zasadzinski, J.; Osmun, J. W.; Wolf, E. L. Proximity Electron Tunneling Spectroscopy. II. Effects of the Induced N-Metal Pair Potential on Calculated S-Metal Properties. *J. Low Temp. Phys.* **1980**, *40* (3), 225−246.
(34) Scoles, G.; Bassi, D.; Buck, U.; Laine, D. *Atomic and Molecular Beam Methods*; Oxford University Press, 1988; Vol. *1*.
(35) Morse, M. Supersonic Beam Sources. In *Atomic, Molecular, and Optical Physics: Atoms and Molecules*, Experimental Methods in the Physical Sciences; Academic Press: Department of Chemistry, University of Utah: Salt Lake City, UT, 1996; Vol. *29B*, pp 21−47.
(36) Scoles, G.; Laine, D.; Valbusa, U. *Atomic and Molecular Beam Methods*; Oxford University Press, 1992; Vol. *2*.
(37) Ekkehard, H.; Ed. *Helium Atom Scattering from Surfaces*; Springer-Verlag: Berlin, 1992; Vol. *27*.
(38) Kress, W.; de Wette, F. W. *Surface Phonons*, Springer Series in Surface Sciences; Springer-Verlag: Berlin, 1991.
(39) Holst, B.; Alexandrowicz, G.; Avidor, N.; Benedek, G.; Bracco, G.; Ernst, W. E.; Farias, D.; Jardine, A. P.; Lefmann, K.; Manson, J. R.; Marquardt, R.; Miret Artés, S.; Sibener, S. J.; Wells, J. W.; Tamtögl, A.; Allison, W. Material Properties Particularly Suited to Be Measured with Helium Scattering: Selected Examples from 2D Materials, van Der Waals Heterostructures, Glassy Materials, Catalytic Substrates, Topological Insulators and Superconducting Radio Frequency Materials. *Phys. Chem. Chem. Phys.* **2021**, *23* (13), 7653−7672, DOI: 10.1039/D0CP05833E.
(40) Anemone, G.; Taleb, A. A.; Benedek, G.; Castellanos-Gomez, A.; Farías, D. Electron−Phonon Coupling Constant of 2H-MoS2(0001) from Helium-Atom Scattering. *J. Phys. Chem. C* **2019**, *123* (6), 3682−3686.
(41) Anemone, G.; Garnica, M.; Zappia, M.; Aguilar, P. C.; Al Taleb, A.; Kuo, C.-N.; Lue, C. S.; Politano, A.; Benedek, G.; de Parga, A. L. V.; et al. Experimental Determination of Surface Thermal Expansion and Electron−Phonon Coupling Constant of 1T-PtTe $_2$. *2D Mater.* **2020**, *7* (2), No. 025007.
(42) Benedek, G.; Manson, J. R.; Miret-Artés, S. The Electron−Phonon Coupling Constant for Single-Layer Graphene on Metal Substrates Determined from He Atom Scattering. *Phys. Chem. Chem. Phys.* **2021**, *23* (13), 7575−7585, DOI: 10.1039/D0CP04729E.
(43) Benedek, G.; Bernasconi, M.; Bohnen, K.-P.; Campi, D.; Chulkov, E. V.; Echenique, P. M.; Heid, R.; Sklyadneva, I. Yu.; Toennies, J. P. Unveiling Mode-Selected Electron−Phonon Interactions in Metal Films by Helium Atom Scattering. *Phys. Chem. Chem. Phys.* **2014**, *16* (16), 7159−7172, DOI: 10.1039/C3CP54834A.
(44) Benedek, G.; Miret-Artés, S.; Manson, J. R.; Ruckhofer, A.; Ernst, W. E.; Tamtögl, A. Origin of the Electron−Phonon Interaction

of Topological Semimetal Surfaces Measured with Helium Atom Scattering. *J. Phys. Chem. Lett.* **2020**, *11* (5), 1927−1933.
(45) Benedek, G.; Manson, J. R.; Miret-Artés, S. The Electron−Phonon Interaction of Low-Dimensional and Multi-Dimensional Materials from He Atom Scattering. *Adv. Mater.* **2020**, *32* (25), No. 2002072.
(46) Tamtögl, A.; Kraus, P.; Avidor, N.; Bremholm, M.; Hedegaard, E. M. J.; Iversen, B. B.; Bianchi, M.; Hofmann, P.; Ellis, J.; Allison, W.; et al. Electron-Phonon Coupling and Surface Debye Temperature of Bi 2 Te 3 (111) from Helium Atom Scattering. *Phys. Rev. B* **2017**, *95* (19), No. 195401.
(47) Sklyadneva, I. Yu.; Benedek, G.; Chulkov, E. V.; Echenique, P. M.; Heid, R.; Bohnen, K.-P.; Toennies, J. P. Mode-Selected Electron-Phonon Coupling in Superconducting Pb Nanofilms Determined from He Atom Scattering. *Phys. Rev. Lett.* **2011**, *107* (9), No. 095502.
(48) Benedek, G.; Toennies, J. P. *Atomic Scale Dynamics at Surfaces Theory and Experimental Studies with Helium Atom Scattering*, Springer Series in Surface Sciences; Springer-Verlag GmbH, Germany, part of SPringer Nature, 2018; Vol. *63*.
(49) Manson, J. R.; Benedek, G.; Miret-Artés, S. Electron−Phonon Coupling Strength at Metal Surfaces Directly Determined from the Helium Atom Scattering Debye−Waller Factor. *J. Phys. Chem. Lett.* **2016**, *7* (6), 1016−1021.
(50) Manson, J. R.; Benedek, G.; Miret-Artés, S. Correction to "Electron−Phonon Coupling Strength at Metal Surfaces Directly Determined from the Helium Atom Scattering Debye−Waller Factor. *J. Phys. Chem. Lett.* **2016**, *7* (9), 1691.
(51) Esbjerg, N.; Nørskov, J. K. Dependence of the He-Scattering Potential at Surfaces on the Surface-Electron-Density Profile. *Phys. Rev. Lett.* **1980**, *45* (10), 807−810.
(52) Gans, B.; Knipp, P. A.; Koleske, D. D.; Sibener, S. J. Surface Dynamics of Ordered Cu3Au(001) Studied by Elastic and Inelastic Helium Atom Scattering. *Surf. Sci.* **1992**, *264* (1), 81−94.
(53) Niu, L.; Gaspar, D. J.; Sibener, S. J. Phonons Localized at Step Edges: A Route to Understanding Forces at Extended Surface Defects. *Science* **1995**, *268* (5212), 847−850.
(54) McMillan, A. A.; Thompson, C. J.; Kelley, M. M.; Graham, J. D.; Arias, T. A.; Sibener, S. J. A Combined Helium Atom Scattering and Density-Functional Theory Study of the Nb(100) Surface Oxide Reconstruction: Phonon Band Structures and Vibrational Dynamics. *J. Chem. Phys.* **2022**, *156* (12), No. 124702.
(55) Payne, M. C.; Teter, M. P.; Allan, D. C.; Arias, T. A.; Joannopoulos, J. D. Iterative Minimization Techniques for Ab Initio Total-Energy Calculations: Molecular Dynamics and Conjugate Gradients. *Rev. Mod. Phys.* **1992**, *64* (4), 1045−1097.
(56) Sundararaman, R.; Letchworth-Weaver, K.; Schwarz, K. A.; Gunceler, D.; Ozhabes, Y.; Arias, T. A. JDFTx: Software for Joint Density-Functional Theory. *SoftwareX* **2017**, *6*, 278−284.
(57) Schlipf, M.; Gygi, F. Optimization Algorithm for the Generation of ONCV Pseudopotentials. *Comput. Phys. Commun.* **2015**, *196*, 36−44.
(58) Perdew, J. P.; Ruzsinszky, A.; Csonka, G. I.; Vydrov, O. A.; Scuseria, G. E.; Constantin, L. A.; Zhou, X.; Burke, K. Restoring the Density-Gradient Expansion for Exchange in Solids and Surfaces. *Phys. Rev. Lett.* **2008**, *100* (13), No. 136406.
(59) Sundararaman, R.; Arias, T. A. Regularization of the Coulomb Singularity in Exact Exchange by Wigner-Seitz Truncated Interactions: Towards Chemical Accuracy in Nontrivial Systems. *Phys. Rev. B* **2013**, *87* (16), No. 165122.
(60) Veit, R. D.; Kautz, N. A.; Farber, R. G.; Sibener, S. J. Oxygen Dissolution and Surface Oxide Reconstructions on Nb(100). *Surf. Sci.* **2019**, *688*, 63−68.
(61) Brown, A. M.; Sundararaman, R.; Narang, P.; Goddard, W. A.; Atwater, H. A. Nonradiative Plasmon Decay and Hot Carrier Dynamics: Effects of Phonons, Surfaces, and Geometry. *ACS Nano* **2016**, *10* (1), 957−966.
(62) Miyake, T.; Oodake, I.; Petek, H. Lateral Thermal Expansion of Cu(110) Surface Studied with Helium Atom Scattering. *Surf. Sci.* **1999**, *427−428*, 39−43.
(63) Farias, D.; Rieder, K.-H. Atomic Beam Diffraction from Solid Surfaces. *Rep. Prog. Phys.* **1998**, *61* (12), 1575.
(64) Levi, A. C.; Suhl, H. Quantum Theory of Atom-Surface Scattering: Debye-Waller Factor. *Surf. Sci.* **1979**, *88* (1), 221−254.
(65) Henzler, M. LEED Studies of Surface Imperfections. *Appl. Surf. Sci.* **1982**, *11−12*, 450−469.
(66) Lapujoulade, J.; Lejay, Y.; Armand, G. The Thermal Attenuation of Coherent Elastic Scattering of Noble Gas from Metal Surfaces. *Surf. Sci.* **1980**, *95* (1), 107−130.
(67) Beeby, J. L. The Scattering of Helium Atoms from Surfaces. *J. Phys. C: Solid State Phys.* **1971**, *4* (18), L359.
(68) Dynes, R. C. McMillan's Equation and the Tc of Superconductors. *Solid State Commun.* **1972**, *10* (7), 615−618.
(69) Transtrum, M. K.; Catelani, G.; Sethna, J. P. Superheating Field of Superconductors within Ginzburg-Landau Theory. *Phys. Rev. B* **2011**, *83* (9), No. 094505.
(70) Townsend, P.; Sutton, J. Investigation by Electron Tunneling of the Superconducting Energy Gaps in Nb, Ta, Sn, and Pb. *Phys. Rev.* **1962**, *128* (2), 591−595.

https://doi.org/10.1021/acs.jpcc.4c00852
J. Phys. Chem. C 2024, 128, 6149−6157